Comparison of aerosol size distributions, radiative properties, and optical depths determined by aircraft observations and Sun photometers during SAFARI 2000

Jim Haywood,[1] Pete Francis,[1] Oleg Dubovik,[2] Martin Glew,[1] and Brent Holben[2]

[1] The Meteorological Office C-130 aircraft performed a dedicated flight over the Etosha Pan surface-based Aerosol Robotic Network (AERONET) Sun photometer site on 13 September 2000 during the Southern African Aerosol Regional Science Initiative (SAFARI 2000) intensive measurement campaign. Aerosol optical depths at different wavelengths, $\tau_{aer\lambda}$, are derived from in situ measurements of the scattering and absorption coefficients and from various radiometric measurements and compared to those derived from the Sun photometer site. The estimates of $\tau_{aer\lambda}$ from the various measurements are shown to be in good agreement. The exception to this is when $\tau_{aer\lambda}$ is derived from the Passive Cavity Aerosol Spectrometer Probe (PCASP), as this method is shown to be extremely sensitive to the pitch angle of the aircraft; therefore, $\tau_{aer\lambda}$ differs for profile ascents and profile descents. However, the aerosol size distribution measured by the PCASP and derived from the AERONET site are in excellent agreement over the $0.05-1.0$ μm radius range, which contains the majority of the optically active particles. C-130-derived refractive indices and single scattering albedos are also shown to be in excellent agreement with those derived from the AERONET site. The consistency between in situ and remotely sensed data suggests that, for aerosol well mixed in the vertical, data from AERONET may be used with confidence in validating satellite measurements and modeling studies of the radiative properties and effects of aerosols.   *INDEX TERMS:* 0305 Atmospheric Composition and Structure: Aerosols and particles (0345, 4801); 0345 Atmospheric Composition and Structure: Pollution—urban and regional (0305); 0360 Atmospheric Composition and Structure: Transmission and scattering of radiation; 3359 Meteorology and Atmospheric Dynamics: Radiative processes; 3360 Meteorology and Atmospheric Dynamics: Remote sensing; *KEYWORDS:* atmospheric aerosol, biomass burning, SAFARI 2000, Sun photometers, aerosol optical depth

1. Introduction

[2] Aerosols affect the radiative balance of the Earth/atmosphere system via the direct effect whereby they scatter and absorb solar and terrestrial radiation, and via the indirect effect whereby they modify the microphysical properties of clouds thereby affecting the radiative properties and lifetime of clouds. The direct radiative forcing due to anthropogenic aerosols remains difficult to quantify because of the extreme spatial variation of different aerosol species, and because of uncertainties in their physical and radiative properties [e.g., *Ramaswamy et al.*, 2001; *Haywood and Boucher*, 2000]. While aircraft measurements are capable of providing high resolution in situ data, operating costs mean that measurements of aerosol physical and optical properties cannot be made on a routine basis. Remote sensing of aerosol size distributions, radiative properties, and optical depths by satellites and surface-based instrumentation offer enhanced spatial and temporal sampling compared with aircraft data. Thus using independently derived aircraft data to check consistency between the aerosol size distributions and optical depths derived from satellites [e.g., *Haywood et al.*, 2001a], and from surface-based Sun photometer sites [e.g., *Russell et al.*, 1999] is highly desirable to improve confidence in both the remotely sensed and aircraft measurements.

[3] This study presents data from a single flight in the direct vicinity of the Etosha Pan Aerosol Robotic Network (AERONET) site during the Southern African Regional Science Initiative (SAFARI 2000) when the source of the aerosol was predominantly biomass burning. It differs from previous studies as the improved aerosol retrieval algorithm of *Dubovik and King* [2000] is used, which allows determination of the size distributions, refractive indices and single

---
[1]Met Office, Bracknell, UK.
[2]National Aeronautics and Space Administration (NASA) Goddard Space Flight Center, Greenbelt, Maryland, USA.

scattering albedo from the spectral dependence of the aerosol optical depth and the angular distribution of the scattered radiances. Section 2 describes the equipment on the C-130, and section 3 briefly describes the flight pattern that was flown on the day of the comparison. Section 4 describes the chemical composition derived from the flight and uses internal mixing to compute the composite refractive indices which are applied to the measured in situ size distributions to derive the optical properties of the aerosol via Mie scattering theory. Section 5 presents four different methods for estimating the aerosol optical depth at wavelengths λ, $\tau_{aer\lambda}$, and section 6 presents estimates of $\tau_{aer\lambda}$ and the aerosol size distribution derived from the AERONET site. A discussion and conclusions are presented in section 7.

2. Instrumentation

[4] The C-130 was equipped with the standard instrumentation detailed by *Johnson et al.* [2001], the aerosol instrumentation detailed by *Haywood et al.* [2003], and the specialist radiation equipment discussed below.

[5] The aerosol instrumentation consisted of a Passive Cavity Aerosol Spectrometer Probe (PCASP-100X) which measures aerosol size distributions between 0.05 and 1.5 μm radius. As detailed by *Haywood et al.* [2003], the Fast Forward Scattering Spectrometer Probe (FFSSP) was not functioning correctly for the duration of the campaign so aerosol radii larger than 1.5 μm could not be measured. Aerosol chemistry was determined from isokinetic sampling onto filter substrates [*Formenti*, 2003]. Aerosol absorption of radiation of wavelength 0.567 μm was measured with a Radiance Research Particle Soot Absorption Photometer (PSAP). Aerosol scattering was determined at three wavelengths (0.45, 0.55, and 0.70 μm) with a TSI 3563 nephelometer. Corrections were applied to the data from the PSAP to account for inaccuracies in the flow rate, area of exposure of the filter, and absorption artifacts following the analysis of *Bond et al.* [1999]. Corrections to the nephelometer to account for variations from STP and for the truncation of forward-scattered radiation were applied following the results of *Anderson and Ogren* [1998] and *Haywood and Osborne* [2000].

[6] The following radiation equipment was fitted to the C-130. Upward and downward facing Eppley broadband radiometers (BBRs) fitted with clear and red domes with aft mounted obscurers which cover the 0.3–3.0 and 0.7–3.0 μm spectral regions respectively [*Hignett et al.*, 1999; *Haywood et al.*, 2001a, 2001b]. The Meteorological Office Scanning Airborne Filter Radiometer (SAFIRE) was designed to measure radiances in 16 bands across the visible and near-infrared region of the spectrum and was mounted in a pod on the port wing of the C-130 [*Francis et al.*, 1999]. During the detachment, only seven of the channels were operated providing radiances at 0.55, 0.62, 0.87, 1.04, 1.25, 1.61, and 2.01 μm. The measurements described here are made with SAFIRE in the zenith viewing mode. An additional instrument installed on the C-130 is the Short-Wave Spectrometer (SWS) which uses two Carl Zeiss spectrometer modules operating in the spectral range 0.30–0.95 and 0.95–1.70 μm. These are connected via optic fibers to a simple light gathering telescope (half angle 0.75°) viewing through a downward pointing aperture

thereby providing a nadir view. The pixel separation is approximately 0.0033 μm in the 0.30–0.95 μm module and 0.006 μm in the 0.95–1.70 μm module, giving approximate spectral resolutions of 0.010 and 0.018 μm, respectively.

3. Meteorology and Flight Patterns

[7] The C-130 of the UK Met Office was based in Windhoek, Namibia and performed two dedicated flights over the Etosha AERONET site on 6 and 13 September 2000. However, variable amounts of cloud were present during 6 September, so this analysis concentrates on data from 13 September only.

[8] Figure 1 shows an 80 hour back-trajectory analysis using the UK Met Office global and regional model winds. The general cyclonic flow in the Southern African Gyre is evident. Much of the most intense biomass burning is concentrated in Zambia at this time of year and hence the biomass is likely to have been generated over 24 hours previously.

[9] The flight consisted of the following sections which are shown schematically in Figure 2:

1. A stacked profile over the Etosha AERONET site, which included six 5 min straight and level runs (SLRs) in the aerosol layer down to the minimum permitted altitude (MPA) with profile descents in between.

2. SLRs of 10 min duration performed at the MPA orientated into-Sun and down-Sun.

3. A series of four orbits over the Etosha site at the MPA where the aircraft was banked at an angle equal to the solar zenith angle, θ.

4. A profile ascent to above the aerosol layer.

5. A SLR above the aerosol layer.

[10] The MPA varied from approximately 330 m above ground level (agl) when performing SLRs and 1000 m agl when performing banked orbits. The stacked and continuous profiles through the aerosol layer enable determination of the aerosol size distributions via in situ sampling with the PCASP probe and various methods may be used for estimating $\tau_{aer\lambda}$ as described in section 5.

4. Aircraft-Derived Aerosol Chemical Composition, Size Distributions, and Optical Parameters

[11] Filters detecting optically active particles with radii less than 0.65 μm were exposed for the duration of the campaign. Chemical analysis [*Formenti*, 2003; *Haywood et al.*, 2003] suggests the campaign mean biomass aerosol fractional mass fraction is approximately 70% organic matter (OM), 25% inorganic matter, and 5% black carbon (BC). Refractive indices for the aerosol are calculated assuming that the only absorbing component is BC and using the Maxwell–Garnet mixing rule which has been shown to perform relatively well for internal mixtures [*Chỳlek et al.*, 1988]. The composite refractive indices are determined assuming a refractive index of BC of $1.75 - 0.44i$ at 0.55 μm [*World Climate Program* (*WCP*), 1986], and a wavelength independent refractive index for the remaining scattering component of $1.53 - 0i$. A density of BC of 1.7 g cm^{-3} which is similar to the 1.8 g cm^{-3} assumed by *Reid and Hobbs* [1998] and density of 1.35 g
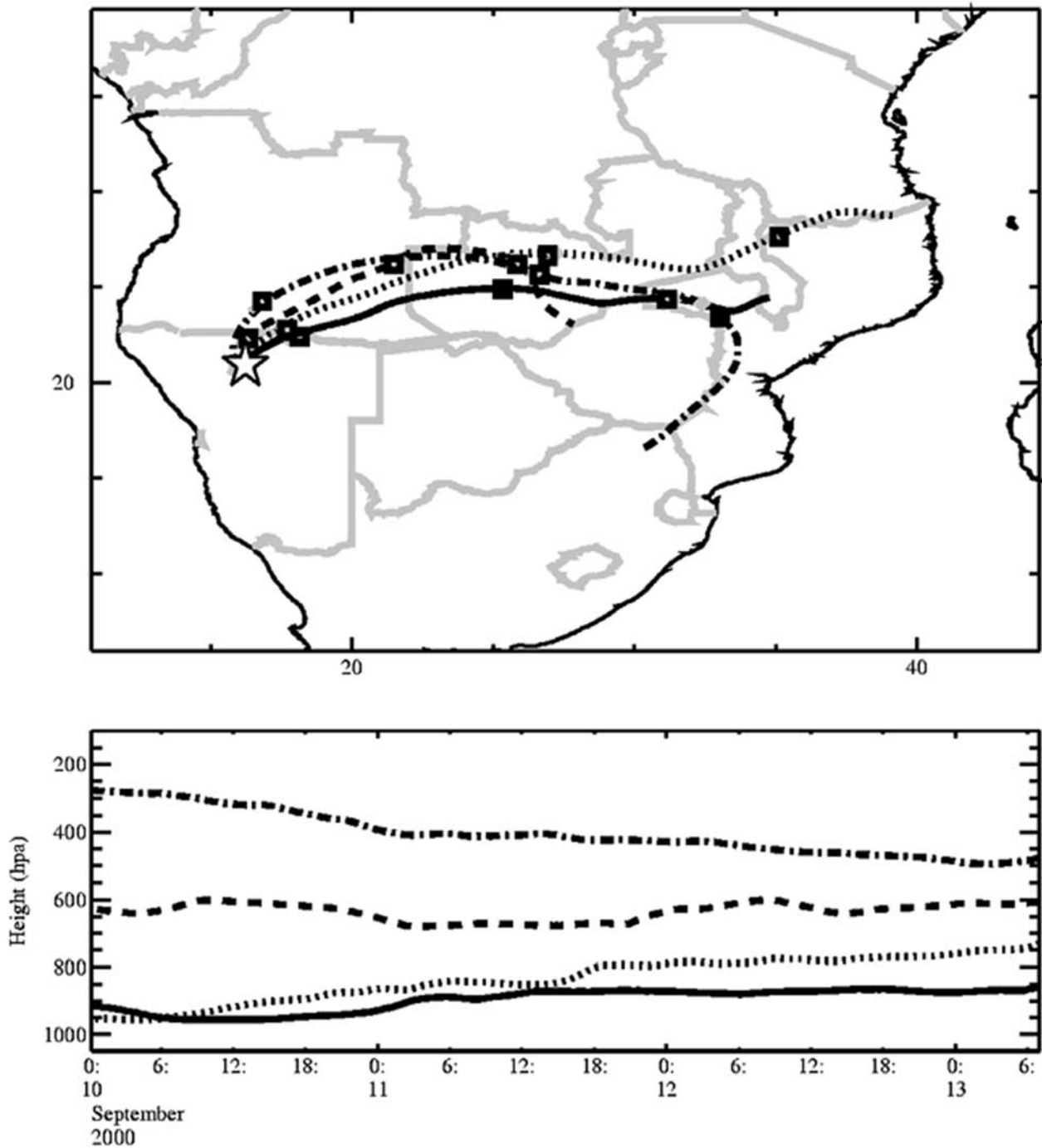
Figure 1. A Met Office 80 hour back-trajectory analysis showing the origin of the aerosol at the Etosha Pan AERONET site on 13 September 2000 (marked with a star). The top panel represents the horizontal back-trajectory analysis and the lower panel the vertical position of the air mass. The squares on the upper panel show the positions of the air mass at 0000 UTC on each day.

cm^{-3} is assumed for the composite aerosol [*Reid and Hobbs*, 1998]. The resulting refractive index for the campaign mean composite biomass aerosol is $1.54 - 0.018i$ at 0.55 μm [*Haywood et al.*, 2003]. This campaign mean refractive index is used in the calculations that follow, although a single filter exposed during the stacked profile descent suggests a BC mass fraction of approximately 7% leading to a modeled refractive index of $1.54 - 0.025i$. The

choice of the campaign mean refractive index of $1.54 - 0.018i$ is justified by independent measurements of ω_o obtained from absorption and scattering measurements as follows.

[12] The aerosol size distributions obtained from the SLRs are shown in Figure 3, which shows that although the aerosol size distributions are similar, the size distributions at higher altitude show a shallower slope in the
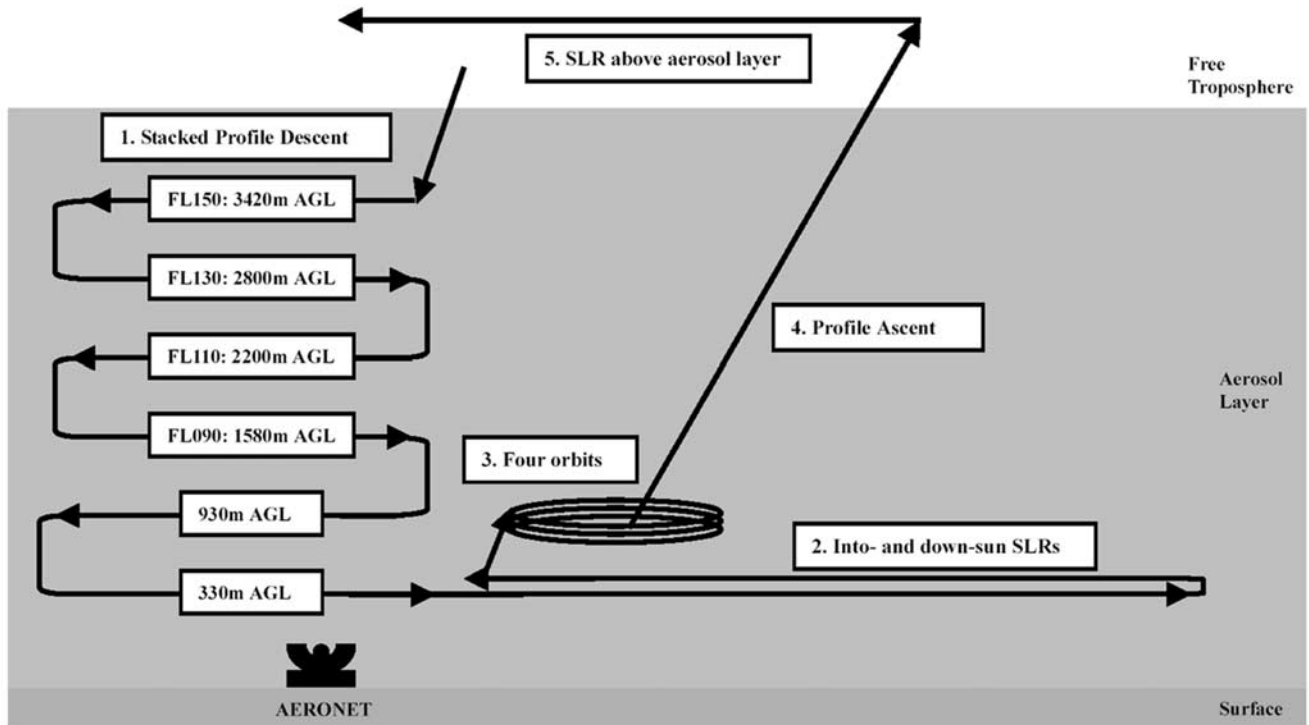
Figure 2. Schematic diagram of the flight pattern performed by the C-130 over the Etosha AERONET site on 13 September 2000. Consisting of (1) stacked profile descent, (2) into-Sun and down-Sun SLRs, (3) a series of four orbits, (4) profile ascent, and (5) SLR above the aerosol layer.

optically active $0.1-0.5$ μm radii region. It is possible that some of the variation in the size distributions is due to particle swelling, as the relative humidity is largest at high altitudes. However, *Kotchenruther and Hobbs* [1998] suggest that the hygroscopic growth for biomass aerosol is much reduced when compared to industrial aerosol, and generally insignificant for relative humidities less than 50%. Table 1 shows that five out of six of the run mean relative humidities are less than 50%. The optical parameters at 0.55 μm were calculated for each of the size distributions shown in Figure 3 using Mie scattering theory and a refractive index of $1.54 - 0.018i$. The results are shown in Table 1. $\omega_{o\lambda=0.55\mu m}$ ranges from 0.90 to 0.88 with a mean of 0.89. Independent measurements of the scattering and absorption coefficients made with the nephelometer and PSAP indicate a $\omega_{o\lambda=0.55\mu m}$ in the range $0.83-0.95$ with a mean of 0.89. Thus, the calculations presented here use the campaign average refractive index of $1.54 - 0.018i$ as this refractive index is in agreement with the independent measurements of the scattering and absorption coefficients.

5. Aircraft Derivation of Aerosol Optical Depth

[13] $\tau_{aer\lambda}$, may be derived from C-130 measurements in five different ways:

1. Measuring the scattering and absorption coefficient using the nephelometer and PSAP and integrating the measurements over height during the profile descent and profile ascent (section 5.1).

2. Measuring the aerosol size distribution using the PCASP and using Mie theory combined with suitable refractive indices to determine the aerosol extinction and integrating the measurements over height during the profile descent and profile ascent (section 5.2).

3. Measuring the direct and diffuse component of the downwelling irradiance from the low-level SLRs with the BBRs and modeling the irradiance in the absence of aerosols (section 5.3) [e.g., *Hignett et al.*, 1999].

4. Measuring the radiance as a function of scattering angle and modeling the aerosol optical parameters and loading necessary to best fit the observations (section 5.4) [*Francis et al.*, 1999].
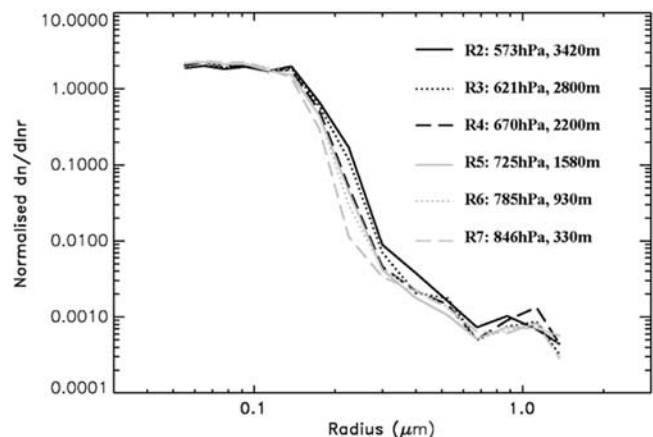
Figure 3. The aerosol size distributions measured by the PCASP-100X during the stacked profile descent shown in Figure 2.

Table 1. The Run Mean Optical Properties of Biomass Burning Aerosols at 0.55 μm[a]

Run Number, Pressure, Altitude	Time (UTC)	Mean RH (%)	$\omega_o(\lambda$ = 0.44, **0.55**, 0.67, 0.87, 1.02 μm)	g	k_e (m² g⁻¹)
R2, 573 hPa, 3420 m	0718:24−0723:25	68.03.2	0.91, **0.90**, 0.88, 0.86, 0.84	0.60	4.16
R3, 621 hPa, 2800 m	0728:54−0733:55	47.60.6	0.91, **0.90**, 0.88, 0.86, 0.83	0.58	4.07
R4, 670 hPa, 2200 m	0739:49−0745:50	33.70.4	0.90, **0.89**, 0.87, 0.84, 0.81	0.57	3.63
R5, 725 hPa, 1580 m	0751:30−0756:30	26.00.6	0.90, **0.89**, 0.87, 0.84, 0.81	0.56	3.60
R6, 785 hPa, 930 m	0801:38−0806:42	21.43.5	0.90, **0.89**, 0.86, 0.84, 0.81	0.55	3.60
R7, 846 hPa, 330 m	0811:45−0817:38	19.61.4	0.90, **0.88**, 0.86, 0.83, 0.80	0.53	3.31
Mean used in calculations			0.90, **0.89**, 0.87, 0.85, 0.82	0.57	3.83

[a]The optical parameters derived from the PCASP probe assume a wavelength-dependent real refractive index similar to the study of *Yamasoe et al.* [1998] (1.54 at 0.55 μm) together with a wavelength-independent imaginary refractive index of $0.018i$ at 0.55 μm and a density of 1.35 g cm⁻³. The specific extinction coefficient refers to the submicron mass. ω_o at a wavelength of 0.55 μm is shown in bold and ω_o is shown at other wavelengths for comparison against those derived from the Sun photometers. The mean aerosol optical parameters are also shown.

5. Measuring the magnitude and spectral dependence of the upwelling radiance from above the aerosol and modeling the aerosol optical parameters and loading to best fit the measurements (section 5.5).

5.1. $\tau_{aer\lambda}$ by Integrating $\sigma_{sca\lambda}$ and $\sigma_{abs\lambda}$ From Nephelometer and PSAP

[14] The nephelometer scattering coefficients, $\sigma_{sca\lambda}$, measured during the stacked profile descent and ascent, were added to the PSAP absorption coefficients, $\sigma_{abs\lambda}$, to determine the extinction coefficients, $\sigma_{ext\lambda}$, as a function of altitude (Figure 4). $\sigma_{abs\lambda}$ is only measured directly at 0.55 μm, so the simple assumption that $\sigma_{abs\lambda}$ is inversely dependent on the wavelength is used to estimate $\sigma_{abs\lambda=0.45}$ and $\sigma_{abs\lambda=0.70}$ [*Haywood et al.*, 2003]. Aerosol extinction below the minimum altitude of the aircraft contributes significantly to the total aerosol extinction and is estimated by simple linear extrapolation.

[15] $\tau_{aer\lambda}$ was then calculated by vertically integrating the extinction coefficient:

$$\tau_{aer\lambda} = \int_0^z \sigma_{ext\lambda}dz \qquad (1)$$

[16] The results from the profile ascent and profile descent are very similar (Table 2) and suggest $\tau_{aer\lambda=0.45}$ = 0.73−0.76, $\tau_{aer\lambda=0.55}$ = 0.53−0.55, and $\tau_{aer\lambda=0.70}$ = 0.32−0.34, the higher value in each case representing the profile ascent and the lower value representing the profile descent.

[17] These optical depths apply to dry biomass aerosol as the nephelometer dries the aerosol on collection with nephelometer relative humidities not exceeding 10% during the profile ascent, while ambient relative humidities reach a maximum of approximately 56%. Application of the range of parameterizations derived by *Kotchenruther and Hobbs* [1998] for biomass aerosol in Brazil increases $\tau_{aer\lambda=0.55}$ by a maximum of less than 2%, indicating that neglect of the effects of relative humidity is justified.

5.2. $\tau_{aer\lambda}$ by Integrating $\sigma_{ext\lambda}$ Derived From the PCASP Size Distribution

[18] $\sigma_{ext\lambda=0.55}$ was also derived as a function of altitude from the mean measured PCASP size distribution and the measured PCASP number concentration. A single aerosol size distribution represented by the mean optical parameters shown in Table 1 was assumed in the calculations. The crosses shown in Figure 4 represent $\sigma_{ext\lambda=0.55}$ from the profile descent and ascent. $\tau_{aer\lambda}$ is then derived using (1). $\tau_{aer\lambda}$ may be derived as a function of wavelength by scaling

σ_{ext} derived from the PCASP size distributions using Mie scattering theory and are summarized in Table 2.

[19] During the profile ascent (Figure 4b), $\sigma_{ext\lambda=0.55}$ derived from the PCASP is significantly lower than that
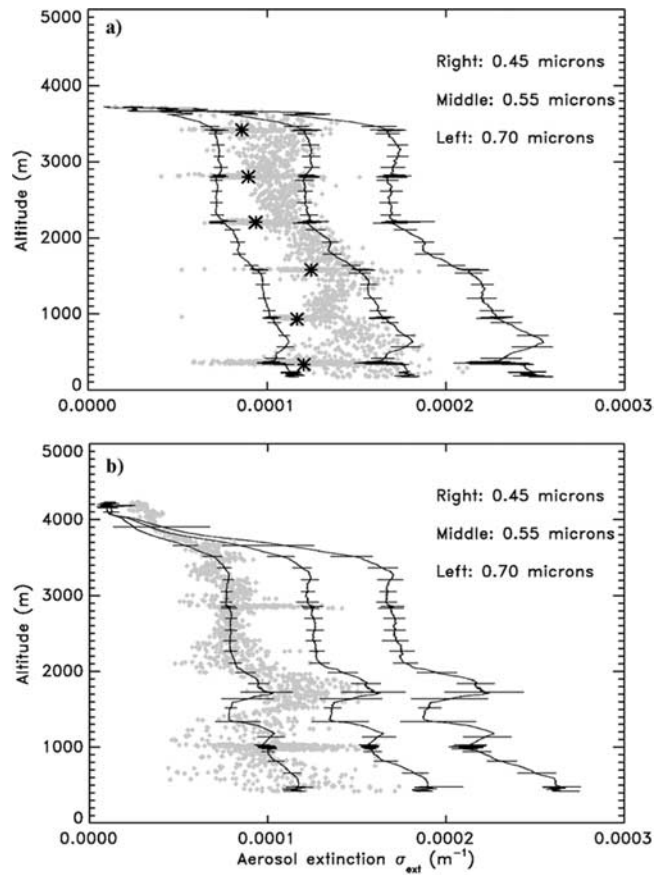
Figure 4. Profiles of σ_{ext} (m⁻¹) derived from the nephelometer and PCASP. (a) Derived from the stacked profile descent and (b) derived from the profile ascent. $\omega_{o\lambda=0.45}$ = 0.90, $\omega_{o\lambda=0.55}$ = 0.89, and $\omega_{o\lambda=0.70}$ = 0.87 as derived from measurements with the nephelometer and PSAP during the stacked profile descent are applied to the nephelometer scattering to determine the extinction coefficient. The vertical lines on σ_{ext} represent the standard deviation in 60 s of nephelometer data. The crosses represent the aerosol extinction coefficient at 0.55 μm derived from the PCASP number concentration. The stars on (a) represent the mean PCASP-derived σ_{ext} and are clearly reduced compared to those from the profile descent.

Table 2. $\tau_{aer\lambda}$ Derived Using the Different Methods Described in the Text for Various Different Wavelengths

Wavelength (μm)	Section 5.1 τ_{aer} PSAP and Nephelometer P1 (Descending)	Section 5.1 τ_{aer} PSAP and Nephelometer P2 (Ascending)	Section 5.2 τ_{aer} PCASP P1 (Descending)	Section 5.2 τ_{aer} PCASP P2 (Ascending)	Section 5.3 τ_{aer} Low-Level SLRs	Section 5.4 τ_{aer} Orbits	Section 5.5 τ_{aer} High-Level SLRs	Section 6.1 τ_{aer} (AERONET)
0.34			0.98	0.78	0.89	1.10	0.98	1.00 ± 0.02
0.38			0.83	0.67	0.76	0.95	0.83	0.88 ± 0.02
0.44			0.67	0.54	0.61	0.76	0.67	0.71 ± 0.01
0.45	0.73	0.76	0.64	0.52	0.59	0.73	0.64	0.69
0.50			0.54	0.43	0.49	0.61	0.54	0.59 ± 0.01
0.55	0.53	0.55	0.46	0.37	0.42	0.52	0.46	0.50
0.67			0.26	0.25	0.30	0.37	0.26	0.35 ± 0.01
0.70	0.32	0.34	0.30	0.24	0.27	0.34	0.30	0.32
0.87			0.22	0.18	0.19	0.24	0.22	0.21 ± 0.01
1.02			0.17	0.14	0.15	0.19	0.17	0.16 ± 0.01

derived from the nephelometer and PSAP as evidenced by the crosses lying well to the left of the middle line which represents $\sigma_{ext\lambda=0.55}$ derived from the nephelometer and PSAP. As a result, $\tau_{aer\lambda=0.55}$ calculated from the profile ascent (P2) is calculated to be 0.38 which is significantly lower than $\tau_{aer\lambda=0.55} = 0.55$ derived from the nephelometer and PSAP (section 5.1 and Table 2). While the agreement is improved during the profile ascent with estimates from the PCASP leading to $\tau_{aer\lambda=0.55} = 0.46$ compared to $\tau_{aer\lambda=0.55} = 0.53$ from the nephelometer and PSAP, there is additional evidence of discrepancies between the profile descent and the SLRs. This is evidenced by the stars lying to the left of the crosses in Figure 4a. These results suggest that the PCASP aerosol number concentration is being affected by differences in the pitch angle of the aircraft which affects the flow around the aircraft disrupting the isokinetic sampling of the wing mounted PCASP. The mean pitch of the aircraft during the profile descent, SLRs and profile ascent was 3.4° (SD 0.5°), 4.8° (SD 0.4°), and 5.8° (SD 0.8°). That these small differences in pitch angle of the aircraft may affect the performance of the PCASP to such an extent is indicative of the difficulties in making in situ aircraft measurements of aerosols.

5.3. $\tau_{aer\lambda}$ by Measuring the Direct and Diffuse Components of the Downwelling Irradiance

[20] $\tau_{aer\lambda=0.3-0.7}$ and $\tau_{aer\lambda=0.7-3.0}$ may be estimated from the direct and diffuse downwelling irradiances measured by the BBRs using the method of *Hignett et al.* [1999]. The basis of this method is that a down-Sun and into-Sun SLR are performed at low level. Specially constructed aft-mounted obscurers shade the clear and red-domed BBRs from direct solar radiation on the down-Sun leg; therefore essentially only the diffuse component of the radiation is measured (subsequent to a correction for radiation scattered in the forward direction that is blocked by the obscurers). This enables derivation of the measured direct irradiance in the presence of aerosols, $Sflx_{aer\lambda}$. Model calculations with the *Edwards and Slingo* [1996] radiation code using the Eddington solver provide estimates of the direct irradiance without aerosols $Sflx_{no\,aer\lambda}$. The aerosol optical depth may then be estimated using the equation [*Haywood et al.*, 2001b]:

$$\tau_{aer\lambda} = \ln\left(\frac{Sflx_{no\,aer\lambda}}{Sflx_{aer\lambda}}\right)\cos\theta \qquad (2)$$

[21] $\tau_{aer\lambda=0.3-0.7}$ above the aircraft was found to be 0.44 while $\tau_{aer\lambda=0.7-3.0}$ was found to be 0.15. The mean altitude

of the C-130 during the down-Sun and into-Sun runs was 380 m (SD 35 m). Examination of the nephelometer scattering profiles shown in Figure 4 suggests that 5–8% of the aerosol optical depth is below the altitude of the aircraft leading to an estimated $\tau_{aer\lambda=0.3-0.7}$ of 0.47 and a $\tau_{aer\lambda=0.7-3.0}$ of 0.16. As in section 5.2, the size distributions shown in Figure 3 are combined to obtain a single aerosol size distribution, which represents the mean optical properties of the aerosol in the atmospheric column (Table 1). $\tau_{aer\lambda}$ at different wavelengths may then be estimated by matching the measured and modeled $Sflx_{aer\lambda=0.3-0.7}$ by adjusting the aerosol loading in a four-stream version of the *Edwards and Slingo* [1996] radiation code. This code was configured to include Rayleigh scattering, absorption by water vapor, carbon dioxide, ozone, and oxygen, the water vapor continuum, and aerosol. Vertical profiles of ozone, water vapor and aerosol are included from the aircraft measurements, while climatological values are used for ozone and oxygen. The resulting aerosol optical depths at different wavelengths are shown in Table 2.

5.4. $\tau_{aer\lambda}$ by Measuring the Spectral Distribution of the Downwelling Radiance as a Function of Scattering Angle

[22] The C-130 performed a series of 4 orbits at approximately 1000 m agl banked at an angle approximately equal to the solar zenith angle, θ, as described by *Francis et al.* [1999]. The radiance was measured for a range of scattering angles from 0° to 2θ° using the SAFIRE instrument (section 2). A single aerosol size distribution was determined from the runs performed above 1000 m agl (R2–R6). The aerosol size distributions from each of the runs was weighted by the approximate contribution to the total aerosol optical depth. A new radiance version of the radiation code developed by *Edwards and Slingo* [1996] was used to model the spectral radiances in the discrete SAFIRE wavelengths. The radiance code was configured to included the radiative components described in section 5.3. The aerosol phase function was represented by 201 moments of the Mie scattering phase function. The vertical profile of aerosol extinction was fixed to be the same as that shown in Figure 4b. The aerosol extinction was scaled keeping the vertical profile fixed so that the measured radiances agree best with the modeled radiances providing the best estimate of $\tau_{aer\lambda}$. Figures 5a and 5b correspond to modeled radiances excluding aerosol and modeled radiances including the aerosol. The range of scattering angles considered is limited to scattering angles
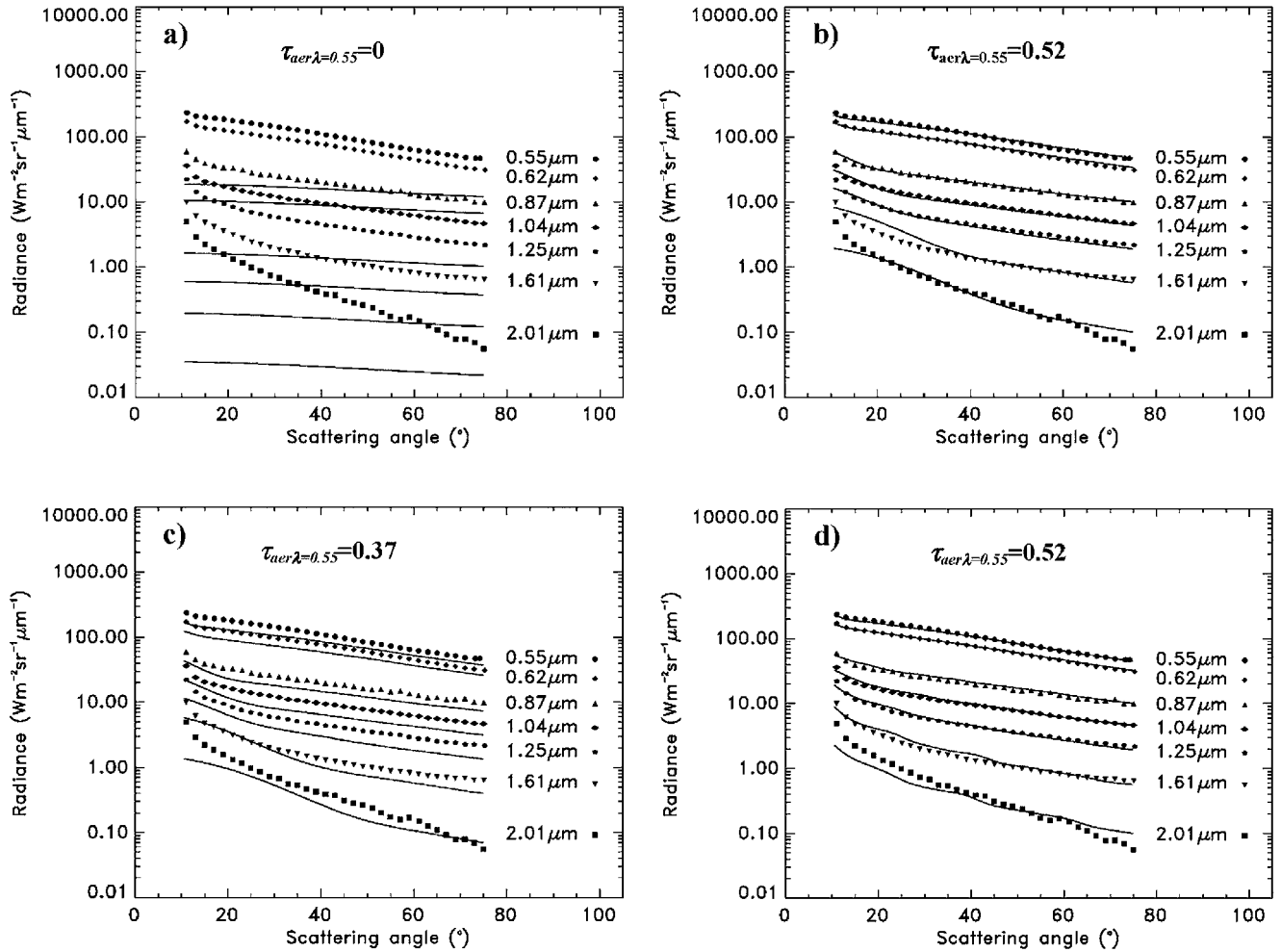
Figure 5. The radiance as a function of the scattering angle for the seven different wavelengths measured by the SAFIRE instrument. The symbols show the measurements and are identical on each of the four panels. The lines show the model calculated radiances for (a) no aerosol, (b) aerosol derived from the PCASP size distribution with $\tau_{aer\lambda=0.55} = 0.52$, (c) aerosol derived from the PCASP size distribution with $\tau_{aer\lambda=0.55} = 0.37$, and (d) aerosol derived from the AERONET size distribution at 0709 UTC with $\tau_{aer\lambda=0.55} = 0.52$. In each case, the solid line showing the highest model radiance is the shortest wavelength, and the line showing the smallest model radiance is the longest wavelength.

greater than 10° owing to SAFIRE calibration limitations when observing a wide range of radiances; the SAFIRE radiances are unreliable when the instrument is pointed directly towards the Sun. The filled symbols show the measured SAFIRE radiances and the solid lines show the model radiances. It is immediately apparent that the measured radiances cannot be modeled if aerosol is excluded from the calculations. Both the absolute magnitude and the slope of the radiances are poorly represented when aerosol is not accounted for. Inclusion of aerosol with $\tau_{aer\lambda=0.55} = 0.52$ leads to very much improved agreement in both the absolute magnitude and the slope of the radiances. The agreement is particularly good for the shorter wavelengths (0.55–1.25 μm), while some more significant differences occur at longer wavelengths (1.61–2.01 μm). This may be understood by considering that the maximum aerosol Mie scattering efficiency occurs when the particle radius is approximately equal to the wavelength of the incident radiation. The PCASP only detects particles up to 1.5 μm radius, and therefore does not detect those particles that have most

influence on the scattered radiance at 1.61 and 2.01 μm. $\tau_{aer\lambda}$ for the SAFIRE wavelengths and the wavelengths of the AERONET Sun photometers and nephelometer are shown in Table 2.

[23] Figure 5c shows modeled radiances when $\tau_{aer\lambda=0.55} = 0.37$. These calculations were performed because this $\tau_{aer\lambda}$ is representative of that derived from the PCASP during the profile ascent. Significant differences exist between the measured and modeled radiances in this case, and are suggestive that the PCASP does not perform well during profile ascent owing to the pitch of the aircraft influencing the flow around the PCASP. During profile descent, when the pitch of the aircraft is reduced, the PCASP gives estimates of $\tau_{aer\lambda}$ that are more consistent with the radiometric measurements.

5.5. $\tau_{aer\lambda}$ by Measuring the Magnitude and Spectral Distribution of the Upwelling Radiance

[24] While *Haywood et al.* [2001a, 2001b] estimated $\tau_{aer\lambda}$ from upwelling irradiances measured by the BBRs

over ocean, $\tau_{aer\lambda}$ cannot be readily estimated by this method in this study due to variability of the surface reflectance. Here, the SWS instrument is used in place of the BBRs to estimate the spectral dependence and magnitude of the surface reflectance, from the low-level runs, and this is used in modeling the upwelling radiance for the high-level SLR.

[25]   The mean measured nadir view radiance at low level from the into-Sun SLR is modeled using the *Edwards and Slingo* [1996] radiation code by adjusting the spectral dependence of the Lambertian surface reflectance, R_s, until the measured and modeled radiances agree. The vertical profile of aerosol is included from the aircraft measurements. The magnitude of the aerosol concentration is then adjusted so that the best agreement is found between the measured and modeled nadir view radiance during the high-level SLR. This method involves a degree of iteration:

1. Guess the aerosol mass loading
2. Guess the surface reflectance
3. Calculate the upwelling radiance at low level
4. Compare the results from 3 against the measurements
5. Adjust the surface reflectance so that the upwelling radiances at low level agree
6. Calculate the upwelling radiance for high-level SLR
7. Compare the modeled upwelling radiance at high level to that measured
8. Adjust the aerosol optical depth
9. Use the new R_s and $\tau_{aer\lambda}$ in steps 3–7.

Implicit within these calculations is the assumption that R_s during the low-level SLR and the high-level SLR are identical. While efforts were made to ensure that the type of surface overflown during the two runs was similar, exact colocation of the two SLRs was not possible. In any case, even if precisely the same track were flown, the footprint of SWS instrument during the high-level SLR is calculated to be approximately 18 times that during the low-level SLR. An additional assumption is that the surface may be modeled using a Lambertian reflector and that the nature of the Bidirectional Reflection Distribution Function (BRDF) is such that the reflected zenith radiance does not change significantly between the low-level SLR ($\theta = 40.6°$), and the high-level SLR ($\theta = 31.0°$).

[26]   Figure 6 shows the measured spectral radiances and the variability in the measurements for the wavelength range 0.4–0.7 μm for the high-level SLR. The variability is clearly evident and is mainly due to the variable nature of R_s. Also shown are calculations excluding and including aerosol for $\tau_{aer\lambda=0.55}$ of 0.37 and 0.5 which approximately represent the minimum and maximum derived from the techniques detailed in sections 5.1, 5.2, and 5.3. The radiances excluding aerosol are different for the following reason. The R_s needed to match the upward radiances of the low-level SLR differ because the $\tau_{aer\lambda}$ applied to the model affects the downwelling radiation at the surface. Thus, it is the different R_s that cause the difference in the upwelling radiance when aerosol is excluded.

[27]   It can clearly be seen that neither of the model calculations excluding aerosol represents the measured radiance for wavelengths less than 0.6 μm. At longer wavelengths all of the simulations are within the measurements ±1 standard deviation. It can also be seen that $\tau_{aer\lambda=0.55} = 0.50$ is clearly an improvement compared to

$\tau_{aer\lambda=0.55} = 0.37$. The radiances for $\tau_{aer\lambda=0.55} = 0.50$ are generally within the envelope of radiances described by the measurements ±1 standard deviation. The radiances for $\tau_{aer\lambda=0.55} = 0.37$ only start to fall within the measurements ±1 standard deviation when the wavelengths exceed 0.6 μm, where all of the simulations give reasonable agreement with the measurements whether or not aerosol is included in the calculations. $\tau_{aer\lambda=0.55}$ that best matches the measurements is approximately 0.46, although this value leads to some significant differences (to 1 standard deviation) in the modeled and measured radiances at wavelengths less than 0.47 μm.

[28]   It is interesting to note that the modeled radiance excluding aerosols is higher than including aerosols for wavelengths exceeding approximately 0.6 μm regardless of the aerosol optical depth. These calculations also suggest that the radiative forcing switches sign from negative to positive (i.e., that the effect of the aerosol on the planetary albedo changes from an increase to a reduction) for wavelengths exceeding approximately 0.6 μm. This is because the surface reflectance increases as a function of wavelength by over a factor of 4 in the wavelength range 0.4–0.7 μm while ω_o decreases from 0.91 to 0.87. Such a swap-over between positive and negative radiative effect is well documented for partially absorbing aerosols above reflective surfaces for both irradiances [e.g., *Haywood and Shine*, 1995; *Boucher et al.*, 1998], and radiances [*Fraser and Kaufman*, 1985] and has recently been used to deduce ω_o for dust aerosol [*Kaufman et al.*, 2001].

6.   AERONET-Derived Optical Depths, Size Distributions, and Optical Parameters

[29]   The details of the Sun photometer operating principles and network are described by *Holben et al.* [1998]. The CIMEL Sun and sky scanning spectral radiometer used at the Etosha AERONET site is a two detector eight channel (0.34, 0.38, 0.44, 0.50, 0.675, 0.87, 0.94, and 1.02 μm) radiometer designed to measure direct solar and sky radiances with a field of view of approximately 1.2°. Direct solar radiances are measured approximately every 15 min between morning and afternoon and converted to $\tau_{aer\lambda}$ according to algorithms, reference calibrations and corrections discussed by *Holben et al.* [1998] and the cloud screening algorithm of *Smirnov et al.* [2000]. After reprocessing using pre and post field calibrations the estimated accuracy in $\tau_{aer\lambda}$ is 0.01–0.02. Sky radiance scans are made in 0.5° increments through the aureole up to 30° in the backscattered direction in both the principle plane and almucantar directions. The radiances have an estimated absolute accuracy of 3–5%. These observations are made hourly and use $\tau_{aer\lambda}$ and the *Dubovik and King* [2000] inversion to derive particle size distributions, complex index of refraction and single scattering albedo within the accuracy limits defined by *Dubovik et al.* [2000].

6.1. $\tau_{aer\lambda}$ From AERONET

[30] $\tau_{aer\lambda}$ derived from the Sun photometer site are analyzed for the period 0707–0952 UTC which is coincident with the aircraft observations. Eight separate observations are available in this time period each consisting of $\tau_{aer\lambda}$ measured at seven different wavelengths from 0.34 to
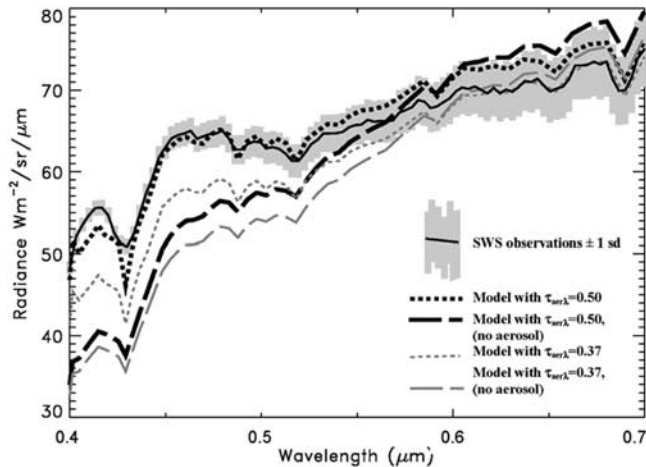
Figure 6. Spectral measurements of the upwelling zenith radiance (nadir view) from the high-level SLR detailed in the text. The dashed lines represent the modeled upwelling radiance without aerosols and differ because different aerosol mass loadings are assumed in deriving the model surface reflectances (see text). The solid lines represent the modeled upwelling radiances for $\tau_{aer\lambda=0.55}$ of 0.37 and 0.50. The agreement between the model and the measurements is clearly better for $\tau_{aer\lambda=0.55}$ of 0.50 than for $\tau_{aer\lambda=0.55}$ of 0.37.

1.02 μm. The data investigated here (available from the Web site http://aeronet.gsfc.nasa.gov) are prefield and postfield campaign calibrated, and have undergone automatic cloud clearing. Table 2 shows that $\tau_{aer\lambda}$ shows very little variation during this time period, the variability in $\tau_{aer\lambda}$ shown in Table 2 being 1 standard deviation. $\tau_{aer\lambda}$ does not vary a great deal even outside the period of operation of the C-130 aircraft as evidenced by $\tau_{aer\lambda=0.50} = 0.61$ (SD 0.03, n = 43) for the full day of measurements.

[31] $\tau_{aer\lambda}$ from the Sun photometers are generally in reasonable agreement with those determined from the radiometric measurements detailed in sections 5.3, 5.4, and 5.5 and somewhat higher than those derived from measuring the in situ scattering and absorption or PCASP number concentrations of the aerosol particles (sections 5.1 and 5.2). The best agreement comes from the comparisons against the measurements of the spectral radiance as a function of scattering angle made by the aircraft (section 5.4).

6.2. Aerosol Size Distribution From AERONET

[32] The retrieval algorithm of *Dubovik and King* [2000] derives the aerosol size distribution from measurements of the spectral optical depth and scattered radiance as a function of scattering angle to retrieve the aerosol size distribution and complex refractive index. The single scattering albedo is then determined from the size distribution and the refractive indices. The measurements presented here are obtained from the six quality controlled size distributions available from the Web site (http://aeronet.gsfc.nasa. gov) for 13 September 2000 for the Etosha Pan. The retrievals are available for 0601, 0623, 0709, 1440, 1526, and 1547 UTC: no retrievals are available closer to local noon as the inversion is only performed when $\theta > 45°$ to maximize the range of scattering angles at which radiances

are measured. We focus our attention on the retrieval at 0709 UTC as this should be most directly comparable with the size distributions derived from the PCASP, and on the mean size distribution from the size retrievals to get some idea of the degree of natural daily variability.

[33] Figure 7 shows the size distribution derived from the inversion algorithm at 0709 UTC plotted as $dV/dlnr$. The thick vertical bars represent $dV/dlnr \pm$ error estimate according to the linear approximation of *Dubovik et al.* [2000]. The shaded gray envelope represents the mean size distribution from the six retrievals ±1 standard deviation and is indicative of the daily natural variability. The daily variability is a larger cause of uncertainty than the estimated error in the size distribution from 0709 UTC. Two different size distributions are shown from the PCASP size distribution. The solid line and the thin vertical bars in Figure 7 is the size distribution derived from the mean PCASP size distribution that is used in the orbit calculations described in section 5. The dotted line shows the PCASP size distribution when a correction is made for the difference in the refractive index between the PCASP calibration latex spheres (1.585 − 0i at the laser wavelength of 0.635 μm). This correction is based on that presented by *Haywood et al.* [2003, Table 1], which assume a refractive index of 1.54 − 0.018i at 0.635 μm. The exception is for the last two bins of the PCASP size distribution which are represented by a refractive index of mineral dust (1.54 − 0.008i at 0.635 μm) [*WCP*, 1986], which is more representative the supermicron aerosol chemistry determined by *Formenti* [2003]. The two size distributions from the PCASP show relatively little difference in the 0.05−0.5 μm size range, but differences become more apparent at larger particle sizes. The size distributions determined from the Sun photometer retrieval algorithm and the in situ measurements are entirely consistent with each other over the radius range 0.05−1.0 μm given the variability/error estimates in the measurements. For radii larger than 1.0 μm, the disagreement between two size distributions increases. *Haywood et al.* [2003] showed that the PCASP-100X sizing of supermicron particles becomes more uncertain due to different scattering responses to ambient aerosol and calibration sphere refractive indices. The retrievals by the Sun photometer are also likely to become less accurate for larger particles [*Dubovik et al.*, 2000] because the radiance measurements are performed up to a maximum wavelength of 1.02 μm. The maximum Mie scattering efficiency occurs when the particle radius is similar to the wavelength of the incident radiation. Therefore, particles of 10 μm radius affect the 1.02 μm scattered radiance to a lesser extent than particles of 1 μm radius. *Dubovik et al.* [2000] estimated that the errors in $dV/dlnr$ do not exceed 10% at the peak of the aerosol size distribution but may reach 35% at the extremes of the size range 0.1−7 μm. Outside these ranges, the errors will increase significantly because of the low sensitivity of the radiances at the measured wavelengths to particles of these sizes.

[34] The effect of using the AERONET-derived size distribution from 0709 UTC in place of the PCASP-derived size distribution is investigated by performing model calculations to determine the distribution of the downwelling scattered radiance as a function of scattering angle as in section 5.4. The results are shown in Figure 5d and reveal a
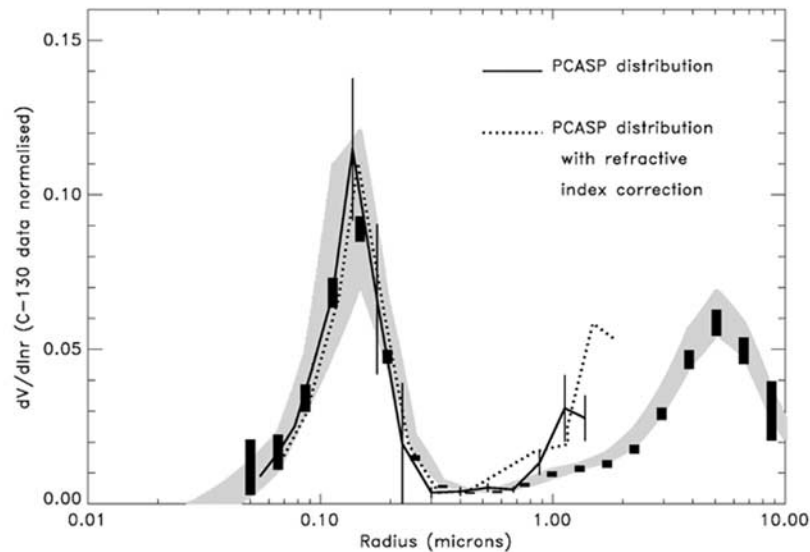
Figure 7. The size distribution derived from the PCASP-100X (black line, with thin vertical lines representing 1 standard deviation in the measurements from the different SLRs). The dotted line represents the PCASP size distribution when differences in the refractive index between the latex calibration spheres and the aerosol are accounted for (see text). The shaded envelope represents the daily mean size distribution ±1 standard deviation derived from the inversion of *Dubovik and King* [2000]. The thick vertical lines represent the size distribution derived at 0709 UTC and include an error estimate for this single size distribution.

good agreement with the measurements. The 1.61 μm radiance at scattering angles between 10° and 35° appears to be better represented by the AERONET size distribution that the in situ PCASP size distribution. The shape of the 2.01 μm radiance also appears to be better represented by the AERONET size distribution. In addition, at small scattering angles close to 10° the stronger peaking of the radiances is better represented by the AERONET size distribution. These differences are due to the in situ PCASP measurements having a maximum detection radius of ~1.5 μm. As noted before, the FSSP probe that measures particles in the radius range 1–23 μm was not functioning properly during the SAFARI 2000 measurement campaign.

6.3. Refractive Index and ω_o From AERONET

[35] The real (*re*) and imaginary (*im*) part of the refractive indices and the single scattering albedo from the *Dubovik and King* [2000] retrievals may also be compared against the C-130 measurements. In the C-130 measurement-based calculations, *re* is 1.53, 1.55, 1.59, and 1.58 at wavelengths of 0.44, 0.67, 0.87, and 1.02 μm, and *im* is 0.018*i* over all these wavelengths (section 4). *re* from the *Dubovik and King* [2000] retrievals is 1.51, 1.54, 1.56, and 1.58 at corresponding wavelengths which is entirely consistent with the C-130 measurements/modeling assumptions given that the variability (1 standard deviation) in the *Dubovik and King* [2000] retrieved *re* is typically 0.05 and the errors quoted by *Dubovik et al.* [2000] are approximately ±0.04. *im* from the *Dubovik and King* [2000] retrieval is 0.020*i*, 0.016*i*, 0.016*i*, and 0.016*i* at wavelengths of 0.44, 0.67, 0.87, and 1.02 μm. This is entirely consistent with the assumption of a wavelength independent *im* of 0.018*i* for the C-130 measurements/modeling given that the variability during the day (1 standard

deviation) in the *Dubovik and King* [2000] derived *im* is 0.002 and the errors quoted by *Dubovik et al.* [2000] are 30%.

[36] The mean ω_o from the *Dubovik and King* [2000] retrieval during the day is 0.88, 0.87, 0.84, and 0.82 at wavelengths of 0.44, 0.67, 0.87, and 1.02 μm. The corresponding ω_o for the mean size distribution used in the calculations derived from the PCASP distributions and from the nephelometer and PSAP on the C-130 is 0.90, 0.87, 0.85, and 0.82 (Table 1). These values for ω_o are entirely consistent with those derived from the *Dubovik and King* [2000] retrieval if one considers the variability (1 standard deviation) in the retrievals during the day is typically 0.01 and the errors quoted by *Dubovik et al.* [2000] are typically ±0.03.

7. Discussion and Conclusions

[37] The optical depths derived from the various different aircraft measurement techniques yields $\tau_{aer\lambda=0.55}$ in the range 0.37–0.55. The smallest $\tau_{aer\lambda=0.55}$ is obtained from integrating σ_{ext} derived from the PCASP. $\tau_{aer\lambda=0.55}$ obtained by integrating σ_{ext} from the PCASP differs depending on whether the aircraft is performing a profile ascent or a profile descent. Thus, it appears that the PCASP number concentration is significantly affected by changes in the pitch of the aircraft by as little as 2.5°. Given the number of independent measurements suggesting a $\tau_{aer\lambda=0.55}$ of approximately 0.50, it is likely that the PCASP number concentration is more accurate while in profile descent which is reasonable as the pitch of the aircraft is smallest. Whatever the cause of this inconsistency, the problems of making in situ aircraft measurements of aerosols are clearly demonstrated.

[38] $\tau_{aer\lambda=0.55}$ for the radiometric measurements detailed in sections 5.2, 5.3, 5.4, and 5.5 lie in the range 0.42–0.52, the smallest being from estimates of the direct and diffuse components of the downwelling irradiance from the low-level SLRs, and the largest being due to estimates from the orbits. These measurements are in good agreement with the $\tau_{aer\lambda=0.55}$ of approximately 0.50 derived from the AERONET Sun photometer site. The uncertainty in the aircraft measurements of the aerosol optical depth varies depending upon the method used. The optical depth from the downwelling irradiances at SLRs at 17 m above the ocean was estimated by *Hignett et al.* [1999] to be uncertain to ±0.03. However, in our case, the altitude of the aircraft was 380 m agl, and there is additional uncertainty associated with the aerosol optical depth below the operating altitude. Additionally the use of 10 min down-Sun and into-Sun runs means that the aircraft covers a horizontal distance of some 60 km and the spatial homogeneity of the aerosol over these distances cannot be guaranteed. Thus, we estimate an uncertainty of at least ±0.05. $\tau_{aer\lambda=0.55}$ for the orbits is subject to uncertainties in the measured radiances, and uncertainties in the aerosol optical depth below the level of the orbits (1000 m agl). However, the uncertainties in the aerosol optical depth below the orbits are corrected for by assuming the aerosol extinction profile is similar to that shown in Figure 4b. There remains some uncertainty in the aerosol optical depth below the aircraft operating altitude which introduces an estimated uncertainty of some 3% in the derived $\tau_{aer\lambda=0.55}$. Investigation of the sensitivity of $\tau_{aer\lambda=0.55}$ to the lack of inclusion of particles with radii greater than 1.5 μm suggests that this contributes an uncertainty of approximately ±0.03. Additional uncertainties in the absolute radiometric calibration of the SAFIRE channels leads to an overall uncertainty estimated as ±0.07. $\tau_{aer\lambda=0.55}$ = 0.46 obtained from measurements of the upwelling radiance has an estimated uncertainty of approximately ±0.05. This value is obtained somewhat subjectively by examining the spectral consistency between the observed upwelling radiances and the modeled upwelling radiances for different optical depths. The error in this estimate will be significantly smaller over ocean regions where the variability of R_s is reduced and will be the subject of further research.

[39] The main conclusion to be drawn from the comparisons of $\tau_{aer\lambda}$ from aircraft measurements and the AERONET site is that the radiometric measurements and in situ measurements are generally in good agreement, although the method using the PCASP gives a significantly lower $\tau_{aer\lambda}$. The errors in this in situ sampling method evidenced by the inconsistencies in the derived $\tau_{aer\lambda}$ are significantly larger than those obtained from radiometric measurements.

[40] The aerosol size distributions derived from the *Dubovik and King* [2000] retrieval are essentially identical to those derived from the PCASP over the optically active 0.1–1.0 μm radius range when the variability/estimated errors in the measurements are considered. This suggests that although the PCASP may not count the total number of aerosol particles sufficiently accurately, the size distribution is well represented. It also suggests that the retrieval algorithm of *Dubovik and King* [2000] does an excellent job of determining the aerosol size distribution when the aerosol is well mixed in the vertical.

[41] The refractive indices derived from filter measurements and the nephelometer and PSAP suggest a refractive index of $1.54 - 0.018i$ and a ω_o of 0.89 at a wavelength of 0.55 μm. These refractive indices and ω_o are in excellent agreement with those derived from the retrieval algorithm of *Dubovik and King* [2000].

[42] To conclude, the agreement between the Sun photometer and aircraft measurements of optical depth, size distribution, real and imaginary part of the refractive index, and single scattering albedo are good. This consistency between the independent aircraft measurements and Sun photometry measurements increases the confidence that both airborne and surface-based Sun photometry methods can be used to assess aerosol physical and radiative properties accurately. This suggests that data from Sun photometers should be used in assessing estimates of the radiative effect of aerosols from satellite sensors and GCM modeling studies when the aerosol layer is well mixed in the vertical. The performance of the Sun photometer retrievals when aerosols with different optical characteristics exists in different vertical layers is the subject of ongoing research.

References

Anderson, T. L., and J. A. Ogren, Determining aerosol radiative properties using the TSI 3563 integrating nephelometer, *Aerosol Sci. Technol.*, *29*, 57–69, 1998.

Bond, T. C., T. L. Anderson, and D. Campbell, Calibration and intercomparison of filter-based measurements of visible light absorption by aerosols, *Aerosol Sci. Technol.*, *30*, 582–600, 1999.

Boucher, O., et al., Intercomparison of models representing direct shortwave radiative forcing by sulfate aerosols, *J. Geophys. Res.*, *103*, 16,979–16,998, 1998.

Chýlek, P., V. Srivastava, R. G. Pinnick, and R. T. Wang, Scattering of electromagnetic waves by composite spherical particles: Experiment and effective medium approximations, *Appl. Opt.*, *27*, 2396–2404, 1988.

Dubovik, O., and M. King, A flexible inversion algorithm for retrieval of aerosol optical properties from Sun and sky radiance measurements, *J. Geophys. Res.*, *105*, 20,673–20,696, 2000.

Dubovik, O., A. Smirnov, B. N. Holben, M. King, Y. J. Kaufman, T. F. Eck, and I. Slutsker, Accuracy assessment of aerosol optical properties retrieval from AERONET sun and sky radiance measurements, *J. Geophys. Res.*, *105*, 9791–9806, 2000.

Edwards, J. M., and A. Slingo, Studies with a flexible new radiation code, 1, Choosing a configuration for a large scale model, *Q. J. R. Meteorol. Soc.*, *122*, 689–720, 1996.

Formenti, P., Inorganic and carbonaceous aerosols during SAFARI 2000: Chemical characteristics, physical properties, and emission data for smoke from African biomass burning, *J. Geophys Res.*, *108* doi:10.1029/2002JD002408, in press, 2003.

Francis, P. N., P. Hignett, and J. P. Taylor, Aircraft observations and modeling of sky radiance distributions from aerosol during TARFOX, *J. Geophys. Res.*, *104*, 2309–2319, 1999.

Fraser, R. S., and Y. J. Kaufman, The relative importance of aerosol scattering and absorption in remote sensing, *IEEE J. Geosci. Remote Sens.*, *23*, 525–533, 1985.

Haywood, J. M., and O. Boucher, Estimates of the direct and indirect radiative forcing due to tropospheric aerosols: A review, *Rev. Geophys.*, *38*, 513–543, 2000.

Haywood, J. M., and S. R. Osborne, Corrections to be applied to the PSAP and nephelometer for accurate determination of the absorption coefficient, scattering coefficient and single scattering albedo, MRF Tech. Note 31, 2000. (Available from Met Office, Bracknell, UK).

Haywood, J. M., and K. P. Shine, The effect of anthropogenic sulfate and soot aerosol on the clear sky planetary radiation budget, *Geophys. Res. Lett.*, *22*, 603–606, 1995.

Haywood, J. M., P. N. Francis, I. Geogdzhayev, M. Mishchenko, and R. Frey, Comparison of Saharan Dust aerosol optical depth derived using aircraft mounted pyranometers and 2-channel AVHRR retrieval algorithms, *Geophys. Res. Lett.*, *28*, 2393–2396, 2001a.

Haywood, J. M., P. N. Francis, M. D. Glew, and J. P. Taylor, The optical properties and direct radiative effect of Saharan Dust: A case study of two Saharan dust outbreaks using aircraft data, *J. Geophys. Res.*, *106*, 18,417–18,428, 2001b.

Haywood, J. M., S. R. Osborne, P. N. Francis, A. Keil, P. Formenti, M. O. Andreae, and P. H. Kaye, The mean physical and optical properties of biomass burning aerosol measured by the C-130 aircraft during SAFARI-2000, *J. Geophys. Res.*, *108*, doi:10.1029/2002JD002226, in press, 2003.

Hignett, P., J. P. Taylor, and P. N. Francis, Comparison of observed and modeled direct aerosol forcing during TARFOX, *J. Geophys. Res.*, *104*, 2279–2287, 1999.

Holben, B. N., et al., AERONET: A federated instrument network and data archive for aerosol characterization, *Remote Sens. Environ.*, *66*, 1–16, 1998.

Johnson, D. W., et al., An overview of the Lagrangian experiments undertaken during the North Atlantic Aerosol Characterisation Experiment (ACE-2), *Tellus*, *52B*, 290–320, 2001.

Kaufman, Y., D. Tanré, O. Dubovik, A. Karnieli, and L. A. Remer, Absorption of sunlight by dust as inferred from satellite and ground-based remote sensing, *Geophys. Res. Lett.*, *28*, 1479–1483, 2001.

Kotchenruther, R. A., and P. V. Hobbs, Humidification factors of aerosols from biomass burning in Brazil, *J. Geophys. Res.*, *103*, 32,081–32,089, 1998.

Ramaswamy, V., O. Boucher, J. Haigh, D. Hauglustaine, J. M. Haywood, G. Myhre, T. Nakajima, G. Y. Shi, and S. Solomon, Radiative forcing of climate change, in *Climate Change 2001: The Scientific Basis: Contribution of Working Group I to the Third Assessment Report of the Intergovernmental Panel on Climate Change*, edited by J. T. Houghton et al., pp. 349–416, Cambridge Univ. Press, New York, 2001.

Reid, J. S., and P. V. Hobbs, Physical and optical properties of young smoke from individual biomass fires in Brazil, *J. Geophys. Res.*, *103*, 32,013–32,030, 1998.

Russell, P. B., J. M. Livingston, P. Hignett, S. Kinne, J. Wong, A. Chien, R. Bergstrom, P. Durkee, and P. V. Hobbs, Aerosol-induced radiative flux changes off the United States mid-Atlantic coast: Comparison of values calculated from sun-photometer and in-situ data with those measures by airborne pyranometer, *J. Geophys. Res.*, *104*, 2289–2307, 1999.

Smirnov, A., B. N. Holben, T. F. Eck, O. Dubovik, and I. Slutsker, Cloud screening and quality control algorithms for the AERONET data base, *Remote Sens. Environ.*, *73*, 337–349, 2000.

World Climate Program (WCP), A preliminary cloudless standard atmosphere for radiation computation, World Meteorol. Organ., Geneva, Switzerland, 1986.

Yamasoe, M. A., Y. J. Kaufman, O. Dubovik, L. A. Remer, B. N. Holben, and P. Artaxo, Retrieval of the real part of the refractive index of smoke particles from Sun/sky measurements during SCAR-B, *J. Geophys. Res.*, *103*, 31,893–31,902, 1998.

———————————

O. Dubovik and B. Holben, National Aeronautics and Space Administration (NASA) Goddard Space Flight Center, Code 923, Greenbelt, MD 20771, USA. (dubovik@aeronet.gsfc.nasa.gov; brent@aeronet.gsfc.nasa.gov)

P. Francis, M. Glew, and J. Haywood, Meteorological Office, Bracknell, UK. (pete.francis@metoffice.com; martin.glew@metoffice.com; jim.haywood@metoffice.com)